



## Supplementary Materials for

### **An Aharonov-Bohm interferometer for determining Bloch band topology**

L. Duca, T. Li, M. Reitter, I. Bloch, M. Schleier-Smith, U. Schneider\*

\*Corresponding author. E-mail: [ulrich.schneider@lmu.de](mailto:ulrich.schneider@lmu.de)

Published 18 December 2014 on *Science Express*  
DOI: 10.1126/science.1259052

#### **This PDF file includes:**

Supplementary Text

Figs. S1 to S3

References

## Supplementary Text

This appendix provides the theoretical background for our interferometric characterization of band topology in a hexagonal optical lattice and additional experimental details. In Section S.1, we present the theory of the Aharonov-Bohm-type interferometer in momentum space. Section S.2 reviews the origin of the Berry flux in a honeycomb lattice, focusing on a tightbinding model that captures the essential physics. We proceed in Sec. S.3 to a complete description of the honeycomb lattice as realized in our experiment. Finally, in Sec. S.4 we account for effects of the atomic momentum distribution to verify our detailed quantitative understanding of the experimental results. In Sec. S.5, we provide additional experimental details.

### S.1 Aharonov-Bohm Interferometry in 2D Bloch Bands

To form an interferometer in reciprocal space, we combine a magnetic field of magnitude  $B = B_0 + \mathbf{r} \cdot \nabla B$  with an orthogonal acceleration  $\mathbf{a} \perp \nabla B$  of the lattice. The resulting time-dependent Hamiltonian for an atom of magnetic moment  $\mu$  and mass  $m$  is

$$H(t) = \frac{\mathbf{p}^2}{2m} + V[\mathbf{r} - \mathbf{R}(t)] - \mu \mathbf{r} \cdot \nabla B - \mu B_0, \quad (\text{S.1})$$

where  $V(\mathbf{r})$  describes the lattice potential at  $t = 0$  and  $\mathbf{R}(t) = \mathbf{a}t^2/2$ . The dynamics of this Hamiltonian is most conveniently analyzed in a frame co-moving with the lattice, which we enter via a unitary transformation  $U(t) = e^{-i\mathbf{r} \cdot m\mathbf{a}t} e^{i\mathbf{p} \cdot \mathbf{R}(t)}$ , with  $\hbar = 1$ . The time-dependent Schrödinger equation  $i\dot{\Psi} = H(t)\Psi$  can then equivalently be expressed as  $i\dot{\tilde{\Psi}} = \tilde{H}\tilde{\Psi}$ , where  $\tilde{\Psi} = U\Psi$  and

$$\tilde{H} = UHU^\dagger + i\dot{U}U^\dagger = \frac{\mathbf{p}^2}{2m} + V(\mathbf{r}) - \mathcal{F}_\mu \cdot \mathbf{r} + \varepsilon_\mu(t). \quad (\text{S.2})$$

Here,  $\mathbf{p}^2/(2m) + V(\mathbf{r}) \equiv H_0$  is the bare lattice Hamiltonian,  $\mathcal{F}_\mu = \mu\nabla B - m\mathbf{a}$  includes both the magnetic force and the fictitious force experienced by the atoms in the non-inertial lattice frame, and  $\varepsilon_\mu(t) = -\mu[\mathbf{R}(t) \cdot \nabla B + B_0]$  describes the Zeeman energy. The  $\mathbf{R}$ -dependent Zeeman contribution is ideally kept zero by setting the acceleration to be orthogonal to the magnetic field gradient. The effect of the energy  $\mu B_0$  is removed by our spin-echo sequence, provided that the magnetic field is constant over the duration of the experiment. We nevertheless retain  $\varepsilon_\mu$  in our analysis to remain aware of potential sources of experimental error. We omit in Eq. S.2 a kinetic energy offset  $\frac{1}{2}m|\mathbf{a}t|^2$  that is common to both spin states.

The effect of the force  $\mathcal{F}_\mu$  is to induce a translation  $\mathbf{k} \rightarrow \mathbf{k} + \mathcal{F}_\mu t$  in reciprocal space. To verify this, and to calculate the phase acquired in the process, we substitute into the time-dependent Schrödinger equation the ansatz

$$\tilde{\Psi}(t) = e^{i\eta(t)} \psi_{\mathbf{k}_0 + \mathcal{F}_\mu t}^n, \quad (\text{S.3})$$

where  $\psi_{\mathbf{k}}^n(\mathbf{r}) = e^{i\mathbf{k} \cdot \mathbf{r}} u_{\mathbf{k}}^n(\mathbf{r})$  are Bloch wavefunctions satisfying  $H_0 \psi_{\mathbf{k}}^n(\mathbf{r}) = E_n(\mathbf{k}) \psi_{\mathbf{k}}^n(\mathbf{r})$  for the  $n^{\text{th}}$  band. We assume that the force is sufficiently weak to restrict the dynamics to a single band of index  $n = 1$ , a condition satisfied in our experiment (see Sec. S.5). After a time  $\tau$ , the wave function acquires a phase  $\eta = \varphi_{\text{dyn}} + \varphi_{\text{Berry}}$  that generically can include both a dynamical contribution

$$\varphi_{\text{dyn}} = \int_0^\tau [E_1(\mathbf{k} + \mathcal{F}_\mu t) + \varepsilon_\mu(t)] dt \quad (\text{S.4})$$

and the geometric contribution that is our chief interest:

$$\begin{aligned}\varphi_{\text{Berry}} &= i \int_0^\tau \langle u_{\mathbf{k}+\mathcal{F}_\mu t}^1 | \nabla_{\mathbf{k}} | u_{\mathbf{k}+\mathcal{F}_\mu t}^1 \rangle \cdot \mathcal{F}_\mu dt \\ &= i \int_C \langle u_{\mathbf{k}}^1 | \nabla_{\mathbf{k}} | u_{\mathbf{k}}^1 \rangle \cdot d\mathbf{k}.\end{aligned}\tag{S.5}$$

The last equality emphasizes that, in contrast to the dynamical phase,  $\varphi_{\text{Berry}}$  depends *only* on the path  $C$  in reciprocal space and not on the time required to traverse it. Note that for an open path  $C$ , the geometric phase  $\varphi_{\text{Berry}}$  is gauge-dependent, as we are free to redefine the functions  $u_{\mathbf{k}}^n$  by an arbitrary  $\mathbf{k}$ -dependent phase factor. Yet for any closed loop, such as is formed by our full spin-echo sequence (Fig. 2),  $\varphi_{\text{Berry}}$  is an observable, gauge-invariant quantity measuring the enclosed Berry flux (39).

To design an interferometer that measures only the Berry phase  $\varphi_{\text{Berry}}$  without dynamical phase contributions, we exploit the symmetry of the lattice under a reflection  $\hat{\mathbf{x}} \rightarrow -\hat{\mathbf{x}}$ . We choose the magnetic field gradient to lie along  $\hat{\mathbf{x}}$  and the acceleration correspondingly along  $\hat{\mathbf{y}}$ . This ensures that two spin states of opposite magnetic moment sample the same dispersion relation at each point in time:

$$E_1(\mathbf{k} + \mathcal{F}_{|\mu|}t) = E_1(\mathbf{k} + \mathcal{F}_{-|\mu|}t).\tag{S.6}$$

Ideally, the dynamical phase is thus common to both interferometer arms and has no influence on the measurement.

In practice, imperfections in alignment of the magnetic field gradient relative to the lattice, or errors in the relative angles or intensities of the lattice beams, can introduce small dynamical phases that contribute to our experimental uncertainty. For example, for the data in Fig. 2 in the main text, the Zeeman term  $\varepsilon_\mu(t)$  in the dynamical phase  $\varphi_{\text{dyn}}$  coming from an imperfect alignment of the magnetic field gradient increases linearly with the lattice acceleration, and consequently the final quasimomentum  $k_y^{\text{fin}}$ , and is likely a dominant source of systematic error at large  $|k_y^{\text{fin}}|$ . The experimental tolerances on the alignment of the magnetic field gradient are discussed further in Section S.5.

## S.2 Berry Flux in a Hexagonal Lattice: Tight-Binding Model

The origin of the Berry fluxes in the honeycomb lattice can readily be understood in the tight-binding limit, where the lattice may be decomposed into two triangular sublattices that are coupled by nearest-neighbor hopping (Fig. S1A). With the ground-state Bloch wavefunctions of the two sublattices as basis states, the two lowest bands of the honeycomb lattice are described by the Hamiltonian (40)

$$H_{\text{tb}}(\mathbf{k}) = \begin{pmatrix} \Delta/2 & -t_{\mathbf{k}} \\ -t_{\mathbf{k}}^* & -\Delta/2 \end{pmatrix},\tag{S.7}$$

where  $\Delta$  is an energy offset between the sublattices and

$$t_{\mathbf{k}} = J e^{i\mathbf{k}\cdot\mathbf{d}_1} + J e^{i\mathbf{k}\cdot\mathbf{d}_2} + J e^{i\mathbf{k}\cdot\mathbf{d}_3},\tag{S.8}$$

with  $\mathbf{d}_i$  being the nearest-neighbor lattice vectors and  $J$  the hopping amplitude. The eigenstates of  $H_{\text{tb}}$  are spinors  $u_{\mathbf{k}}^\pm$ , which may be visualized in terms of the expectation value  $\mathbf{S}(\mathbf{k}) = \pm \langle u_{\mathbf{k}}^\pm | \boldsymbol{\sigma} | u_{\mathbf{k}}^\pm \rangle$

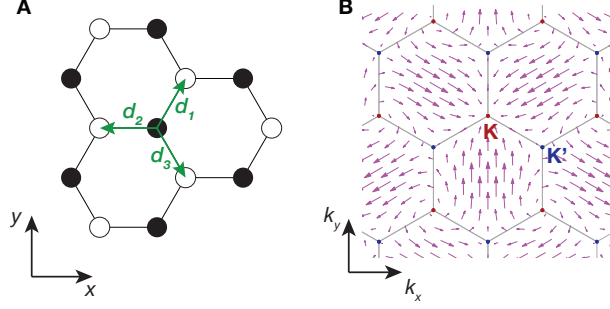


Figure S1: Tight-binding model of the honeycomb lattice. **(A)** Lattice in real space, composed of sub-lattices  $A$  (solid circles) and  $B$  (open circles), with nearest-neighbor hopping vectors  $\mathbf{d}_i$ . **(B)** Spinor eigenstates in reciprocal space, illustrated for the case of degenerate sublattices  $\Delta = 0$ . Directions of the purple arrows indicate the orientation of  $\mathbf{S}(\mathbf{k})$  in the  $x, y$ -plane. Lengths of the arrows indicate the gap  $E_+(\mathbf{k}) - E_-(\mathbf{k})$  between eigenenergies  $E_\pm$  of  $H_{\text{tb}}$ . The winding of  $\mathbf{S}$  about the  $\hat{z}$  axis in the vicinity of each Dirac point  $\mathbf{K}, \mathbf{K}'$  (red, blue) produces a sign change in the wave function of a particle that adiabatically encircles it (41), corresponding to a Berry phase of  $\pi$ .

of the Pauli operator  $\sigma$  in the ground state. The momentum-dependent orientation of the pseudospin  $\mathbf{S}(\mathbf{k})$  is illustrated in Fig. S1B. For  $\Delta = 0$ , the pseudo-spin  $\mathbf{S}$  undergoes a full rotation in the  $S_z = 0$  plane in an infinitesimal loop around a Dirac point. This winding gives rise to the  $\pi$  Berry flux at the Dirac point, in precise analogy to the  $\pi$  phase acquired by a spin-1/2 particle as its alignment adiabatically follows a magnetic field through a single rotation in the  $xy$ -plane (41).

More generally, for an arbitrary two-band system, the Berry curvature of the  $n^{\text{th}}$  band may be calculated as

$$\Omega_n(\mathbf{k}) = i \nabla_{\mathbf{k}} \times \langle u_{\mathbf{k}}^n | \nabla_{\mathbf{k}} | u_{\mathbf{k}}^n \rangle = \frac{\mathbf{S}}{2} \cdot \left( \frac{\partial \mathbf{S}}{\partial k_x} \times \frac{\partial \mathbf{S}}{\partial k_y} \right). \quad (\text{S.9})$$

For the honeycomb lattice with nearly degenerate sublattices ( $\Delta/J \ll 1$ ), as in the case of our experiment,  $\Omega$  is well approximated in the vicinity of each Dirac point  $\mathbf{K}_+ \equiv \mathbf{K}$  or  $\mathbf{K}_- \equiv \mathbf{K}'$  by

$$\Omega_n(\mathbf{k}) \approx \pm \frac{1}{2\gamma^2} \left( 1 + \left| \frac{\mathbf{k} - \mathbf{K}_\pm}{\gamma} \right|^2 \right)^{-3/2}, \quad (\text{S.10})$$

where  $\gamma = \frac{1}{3d} \frac{\Delta}{J}$  parametrizes the distribution of Berry curvature, and  $d = |\mathbf{d}_i|$ . We quantify the spread in Berry curvature in terms of the half-width at half maximum  $\delta k_\Omega$  of the distribution  $\Omega_n(\mathbf{k})$ . In the limit of perfect sublattice degeneracy ( $\Delta = 0$ ), Eq. S.10 reduces to the singular form  $\Omega_n(\mathbf{k}) = \pm \pi \delta(\mathbf{k} - \mathbf{K}_\pm)$ . This singularity is imposed by the symmetries of the lattice under time reversal  $\mathcal{T}$  and inversion  $\mathcal{I}$ , which preclude any loop in reciprocal space from enclosing a Berry flux with a well-defined sign (42).

### S.3 Optical Hexagonal Lattice: Full Description

As our experiments are performed outside the tightbinding regime, we perform all theoretical modeling of the system by *ab initio* band-structure calculations incorporating the full lattice potential.

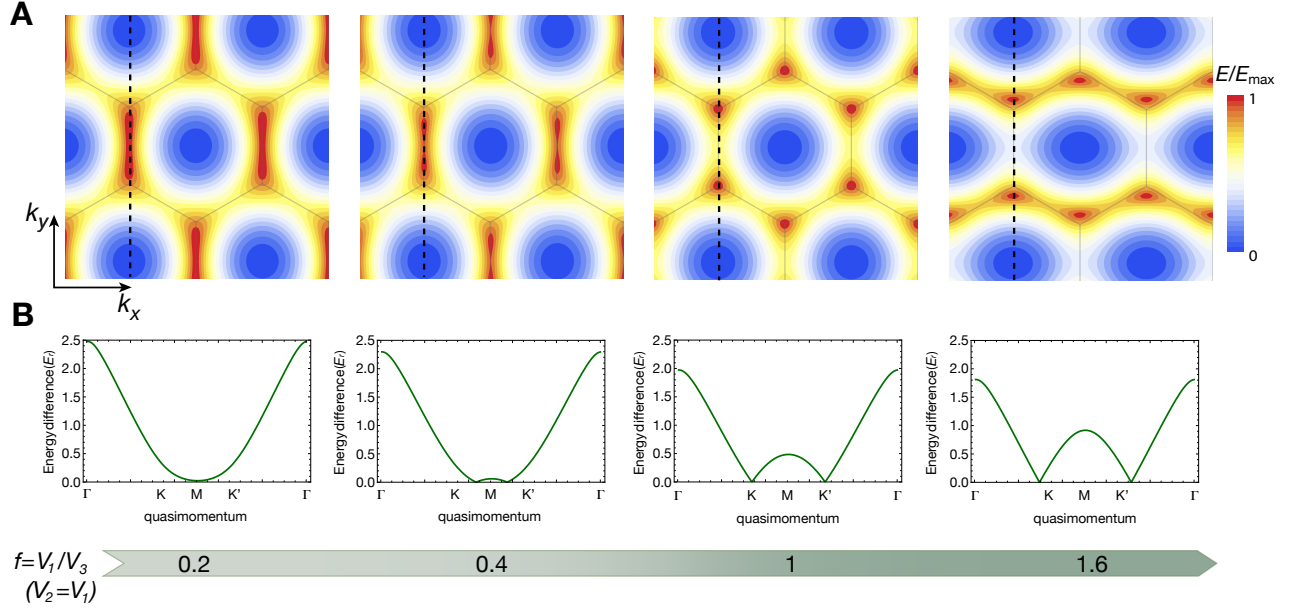


Figure S2: Energy spectrum and movement of the Dirac points. (A) 2D plots of the lowest energy band from *ab initio* calculations as a function of intensity imbalance  $f = V_{1,2}/V_3$ , where  $V_3 = 1 E_r$ . The color scale on each plot is normalized to the band width  $E_{\max}$ . The dashed lines indicate the merging direction which is also the symmetry axis of the interferometer. (B) Energy splitting between the two lowest bands for a cut along the merging direction ( $k_x^{\text{fin}}=0$ ).

The experimental setup described in the main text produces a lattice of the form

$$\begin{aligned}
 V(x, y) &= \left| \sum_{i=1}^3 \sqrt{V_i} e^{-i\mathbf{k}_i \cdot \mathbf{r}} \right|^2 \\
 &= V_1 + V_2 + V_3 + 2\sqrt{V_1 V_2} \cos(\sqrt{3} k_L x) \\
 &\quad + 2\sqrt{V_1 V_3} \cos\left(k_L \left(\frac{\sqrt{3}}{2} x - \frac{3}{2} y\right)\right) \\
 &\quad + 2\sqrt{V_3 V_2} \cos\left(k_L \left(\frac{\sqrt{3}}{2} x + \frac{3}{2} y\right)\right), \tag{S.11}
 \end{aligned}$$

where  $\mathbf{k}_i$  are the wave-vectors of the three lattice beams with wavenumber  $k_L = |\mathbf{k}_i|$  and  $V_i$  is the ac Stark shift produced by the  $i^{\text{th}}$  beam alone. Note that  $V_i \propto I_i$ , where  $I_i$  are the intensities of the beams. All of our experiments are conducted with  $V_1 = V_2$ , so that the lattice is symmetric under reflection  $x \rightarrow -x$  about the symmetry axis of the interferometer. This condition ensures, together with the orthogonality between lattice acceleration and magnetic field gradient, that the interferometer measures only a geometrical phase while dynamical phases cancel out (see Sec. S.1).

i. Imbalanced Lattice

To vary the location of the Berry flux in the reciprocal lattice, we change the intensities of two lattice beams relative to the third, setting  $V_{1,2} = fV_3$ . The lower the imbalance factor  $f$ , the smaller the separation between the Dirac points along the  $\hat{y}$  direction becomes, as illustrated in Fig. S2. At a critically low imbalance factor  $f_c$ , the Dirac points merge and the corresponding Berry fluxes annihilate, leaving a gapped spectrum with no topological features for  $f < f_c$  (43, 44). For the lattice depth of  $1E_r$  employed in our experiments and considered in Fig. S2,  $f_c = 0.2$ .

ii. Calculation of Berry curvature

For the ideal honeycomb lattice defined in Eq. S.11, time-reversal and inversion symmetries dictate that the Berry curvature has to be localized in delta-function singularities. In practice, however, the Berry curvature may be spread out by experimental imperfections that break the inversion symmetry, such as ellipticity in the lattice beam polarizations (45). To allow for a finite Berry curvature in our model, we add to the potential of Eq. S.11 a term

$$V_{AB} = \frac{\Delta}{\sqrt{3}} \sin(\sqrt{3}k_L x) \quad (\text{S.12})$$

that introduces a small energy offset  $\Delta$  between the  $A$  and  $B$  sublattices. By numerically diagonalizing the full Hamiltonian including this term, we calculate the Berry curvature from the eigenstates  $|u_{\mathbf{k}}^n\rangle$  on a discrete grid in reciprocal space (46). Refining the grid via a local adaptive algorithm enables an efficient and precise calculation even for the highly localized Berry curvature in our system. To quantify the localization in Berry curvature and estimate the associated sublattice offset  $\Delta$ , we fit the numerical calculation with the model of Eq. S.10.

### S.4 Effects of Atomic Quasimomentum Distribution

To accurately relate the measured interferometer phases to the location of the Berry flux in reciprocal space, we must account for the quasimomentum spread of the weakly interacting atom cloud. In an interferometer that encloses a region  $S$  for atoms initially at  $\mathbf{k} = 0$ , an atom that instead has an initial quasimomentum  $\mathbf{k} = \mathbf{Q}$  acquires a Berry phase

$$\Phi(\mathbf{Q}) = \int_S \Omega(\mathbf{k} + \mathbf{Q}) d^2\mathbf{k}. \quad (\text{S.13})$$

In our most straightforward analysis, we measure spin-state population fractions ( $n_{\uparrow}, n_{\downarrow}$ ) averaged over the entire cloud to obtain a Ramsey fringe

$$\begin{aligned} n_{\uparrow} - n_{\downarrow} &= \int \cos[\varphi_{MW} + \Phi(\mathbf{Q})] n(\mathbf{Q}) d^2\mathbf{Q} \\ &= \mathcal{C} \cos(\varphi_{MW} + \varphi), \end{aligned} \quad (\text{S.14})$$

where  $n(\mathbf{Q})$  represents the normalized initial quasimomentum distribution, with  $\int n(\mathbf{Q}) d^2\mathbf{Q} = 1$ . The phase  $\varphi = \arg(z)$  and the observed contrast  $\mathcal{C} \leq |z|$  are given by

$$z = \int n(\mathbf{Q}) \exp(i\Phi_{\mathbf{Q}}) d^2\mathbf{Q}. \quad (\text{S.15})$$

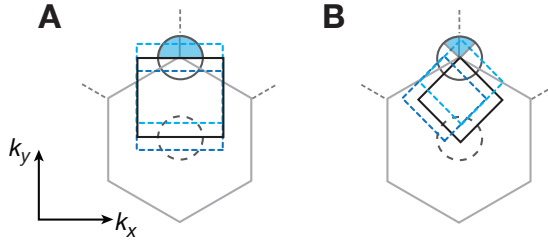


Figure S3: Effect of the geometry of the loop and quasimomentum spread. Examples of interference loops ending at the  $\mathbf{K}$  point with rectangular (**A**), or rhombic (**B**), geometry, illustrating how the shape of the loops affects the fraction of atoms which acquire a phase shift (blue sectors of the circles). Light (dark) blue lines represent paths which have (have not) enclosed the Dirac point. For our interferometer loop (**B**), only a minority of the atoms that cross the edge of the BZ is phase shifted.

The actual interference contrast in the experiment is imperfect due to inhomogeneous broadening of the microwave transition and the heating associated with dynamical instability. In modeling the data, we therefore globally rescale the predicted contrast  $\mathcal{C}$  according to the maximum observed contrast for loops ending close to the Dirac point ( $\Delta k \simeq 0.1 - 0.2 k_L$ ), i.e.,  $\mathcal{C} = \mathcal{C}_{\max} \times |z|$ . We find excellent agreement between this simple model and our data.

Comparisons of experimental results with the above model are shown in Fig. 2-4 of the main text. In calculating each of the model curves in the graphs, we assume  $n(\mathbf{Q})$  to be Gaussian with standard deviation  $\sigma_{\mathbf{k}}$ . In Fig. 2, to account for heating during the sequence, the blue shaded area shows the predicted phase  $\varphi$  vs. final quasimomentum for a range of values  $0.14k_L \leq \sigma_{\mathbf{k}} \leq 0.28k_L$ . The minimum value of  $\sigma_{\mathbf{k}}$  corresponds to the independently measured momentum spread of the cloud before the start of the interferometer sequence of  $\sigma_{\mathbf{k}} = 0.14(1)k_L$  (see the experimental section Sec. i. for details).

As the theory curves illustrate, the position of the phase jump is affected by the momentum spread of the cloud. In the case of a highly localized Berry curvature, this shift can be understood using simple geometric arguments, as it depends only on the distribution of the cloud in reciprocal space and the geometry of the interference loop. The phase jump and the minimum in the interference contrast occur when half of the particles have enclosed the Dirac point at the end of the loop. If the loop has a rectangular shape and its extension is larger than the quasimomentum spread of the cloud, for example, the phase jump will occur exactly at the Dirac point (see Fig. S3A). For our rhombic paths, however, when the interferometer path ends at the  $\mathbf{K}(\mathbf{K}')$  point, only the atoms in the shaded sector of Fig. S3B have performed a loop which enclosed the Dirac point. The shape of this sector of the atomic cloud is given by the opening angle of the loop, which is about  $\sim 70^\circ$  at the first Dirac point, and the fraction of atoms in the sector is determined by the distribution  $n(\mathbf{Q})$ . The data in Fig. 3 and 4A, close to the edge of the BZ, are best fit by a distribution of rms width  $\sigma_{\mathbf{k}} = 0.15k_L$ , consistent with the independently measured value.

#### i. Auxiliary analysis near the Dirac point

The self-referenced interferometry presented in Fig. 3 employs an auxiliary analysis of the images obtained for final quasimomenta in the vicinity of the Dirac point  $\mathbf{K}$ . Here, the edges of the

three Brillouin zones that touch at  $\mathbf{K}$  “slice” the atomic cloud into three components ( $L, R, B$ , as labeled in Fig. 3) that are well spatially separated in band-mapped pictures after time-of-flight (TOF) expansion. We perform independent fits to each of the three corresponding interference fringes to determine the phase

$$\varphi = (\varphi_L + \varphi_R)/2 - \varphi_B. \quad (\text{S.16})$$

Here,  $L$  and  $R$  label the atoms in slices that are first to pass the Dirac point and thereby acquire a phase shift relative to atoms in cloud  $B$ . In modeling the self-referenced interferometer, we apply Eqs. S.14-S.15 to calculate the phase of each interference fringe, substituting for  $n(\mathbf{Q})$  one of the three slices of the full quasi-momentum distribution. The curve calculated for  $\sigma_{\mathbf{k}} = 0.15k_L$  fits the data in both Fig. 3B and Fig. 4B very well.

The data in Fig. 4B are obtained from self-referenced interferometry with paths enclosing up to two Dirac points. In the vicinity of the second Dirac point we again apply Eq. S.16, with the label  $B$  now referring to the contingent of atoms that lead the procession along  $\mathbf{k}_y$  and are thus first to sample the Berry flux of both Dirac points. Theory lines in Fig. 4B are arctangent fits with the slope of the phase jump fixed by our best estimate of the HWHM of the Berry curvature,  $\delta k_{\Omega} \simeq 10^{-4}k_L$ , from the data of Fig. 3B.

## S.5 Experimental methods

Here we provide additional information on the relevant experimental parameters and the optimizations taken to reduce potential sources of errors in the evaluation of the Berry phase.

### i. Preparation scheme

$^{87}\text{Rb}$  atoms are cooled to quantum degeneracy by evaporative cooling initiated in a plugged quadrupole trap and completed in a crossed-beam dipole trap. The experimental sequence begins with an almost pure BEC of typically  $4 \cdot 10^4$  atoms in the internal state  $|F = 1, m_F = 0\rangle$ . The magnetic field gradient is turned on 2s before the interferometer sequence starts to allow the current to stabilize. The atoms are then adiabatically loaded into a hexagonal lattice of chosen depth and configuration in 100 ms. A  $15\mu\text{s}$  microwave  $\pi$ -pulse transfers the atoms in  $|1, 0\rangle$  to  $|2, 1\rangle$  to start the spin-echo sequence.

Directly after loading into the lattice, the momentum spread measured via time of flight expansion is  $\sigma_{\mathbf{k}} = 0.14(1)k_L$ . TOF images after the interferometry sequence show evidence of modest heating over the course of the motion, attributable to dynamical instabilities arising in regions of reciprocal space where the atoms acquire a negative effective mass (47).

### ii. Lattice calibration and trap frequencies

The lattice depth is calibrated via Stückelberg interferometry (48). By measuring the energy difference between the first and second band at different locations in the Brillouin zone (BZ), we estimate a lattice depth of  $1.0(1)E_r$ . The trap frequencies of the combined blue-detuned lattice and dipole potential are  $\omega_{x,y}/2\pi=26.5(7)$  Hz and  $\omega_z/2\pi=183(2)$  Hz. They are obtained by measuring the oscillation frequency of the center-of-mass motion of the BEC after a perturbation of the trapping potential. Due to the modest atom number and the rather small trap frequencies, the system is sufficiently dilute such that interaction effects can be neglected to first order.

### iii. Detection

We perform a band-mapping sequence by linearly ramping down the lattice in  $410 \mu\text{s}$ . During the 10 ms TOF, a Stern-Gerlach pulse of 9.5 ms is applied to separate the  $|\uparrow\rangle$  and  $|\downarrow\rangle$  states. While this imaging can perfectly resolve the  $L$ ,  $R$ ,  $B$  parts in the BZ within each spin component (see Fig. 3A in the main text), due to the short TOF the imaged size of these parts remains dominated by the in situ cloud size and is therefore a convolution of the quasimomentum and real-space distributions. To extract the phase after the interferometry, we count the population of atoms in the two spin states. Depending our analysis method, we count either the atoms in the individual slices ( $L$ ,  $R$ ,  $B$ ) or all the atoms of the cloud.

### iv. Acceleration parameters

In all the experimental runs, the magnetic field gradient produces an acceleration  $|\mu\nabla B|/m=2.9(1) \text{ m/s}^2$ . The frequency of lattice beam three is swept via acousto-optical modulators to accelerate the atoms along the propagation direction of the beam (49). The magnitude of this acceleration is  $|\mathbf{a}| = \frac{2}{3}\lambda_L \frac{d\nu}{dt}$ , where  $\frac{d\nu}{dt}$  is the rate of frequency change,  $\lambda_L=755\text{nm}$ . In the experiment, we vary the lattice acceleration from 1 to  $11 \text{ m/s}^2$  to change the atoms' final quasimomentum  $k_y^{\text{fin}}$ . We quantify the adiabaticity of the motion for this range of forces by checking that the occupation of higher bands is negligible at the end of the interferometry. This is done by bringing the atoms back to the  $\Gamma$ -point, followed by a band-mapping sequence to extract the population of the atoms in the different bands. For interferometer paths ending near the Dirac point, where the adiabaticity condition is hardest to fulfill, the population in the second band is at most  $\sim 20\%$  of the total atom number. We have verified that the excited-band population near the Dirac point does not appreciably affect our measurement by numerically integrating the Schroedinger equation for the two-band model. While the second-band atoms can slightly shift the observed position of the phase jump and the associated dip in contrast, we find no effect of the second-band atoms on the widths of phase jump and contrast dip, from which we obtain bounds on the spread in Berry curvature.

### v. Optimization of the spin-echo sequence

Time-dependent fluctuations of the magnetic field  $B(t)$  are the dominant source of noise in the interferometry sequence and contribute to the dynamical phase (see eq. S.4). To minimize the effect of magnetic field fluctuations, which are mostly due to background AC-noise, we synchronize the beginning of the interferometer sequence to the 50 Hz-line and keep the duration of the sequence fixed at 1.6 ms.

As mentioned in Sec. S.1, the orthogonality of the lattice and gradient force is crucial for the cancellation of dynamical phases, and it is necessary to fine-tune the alignment of the forces. Therefore, to create the gradient, we use both a main coil and a second fine-tuning coil which is roughly perpendicular in position to the main coil. By changing the current through the latter coil, we can tilt the direction of the combined gradient. For orthogonal gradient and lattice forces, the phase measured by the zero-area reference interferometer should be independent of  $k_y^{\text{fin}}$ . Hence, to optimize the direction of the gradient, we measure the phase of the reference loop for different lattice accelerations and currents of the fine-tuning coil. From our calibration, we estimate an error on the gradient alignment of at most  $2^\circ$ .

## References

1. M. V. Berry, Quantal phase factors accompanying adiabatic changes. *Proc. R. Soc. London Ser. A* **392**, 45–57 (1984). [doi:10.1098/rspa.1984.0023](https://doi.org/10.1098/rspa.1984.0023)
2. A. Shapere, F. Wilczek, *Advanced Series in Mathematical Physics: Volume 5, Geometric Phases in Physics* (World Scientific, Singapore, 1989).
3. Y. Aharonov, D. Bohm, Significance of electromagnetic potentials in the quantum theory. *Phys. Rev.* **115**, 485–491 (1959). [doi:10.1103/PhysRev.115.485](https://doi.org/10.1103/PhysRev.115.485)
4. D. Xiao, M.-C. Chang, Q. Niu, Berry phase effects on electronic properties. *Rev. Mod. Phys.* **82**, 1959–2007 (2010). [doi:10.1103/RevModPhys.82.1959](https://doi.org/10.1103/RevModPhys.82.1959)
5. D. J. Thouless, M. Kohmoto, M. P. Nightingale, M. den Nijs, Quantized Hall conductance in a two-dimensional periodic potential. *Phys. Rev. Lett.* **49**, 405–408 (1982). [doi:10.1103/PhysRevLett.49.405](https://doi.org/10.1103/PhysRevLett.49.405)
6. M. Z. Hasan, C. L. Kane, Colloquium: Topological insulators. *Rev. Mod. Phys.* **82**, 3045–3067 (2010). [doi:10.1103/RevModPhys.82.3045](https://doi.org/10.1103/RevModPhys.82.3045)
7. H. Price, N. Cooper, Mapping the Berry curvature from semiclassical dynamics in optical lattices. *Phys. Rev. A* **85**, 033620 (2012). [doi:10.1103/PhysRevA.85.033620](https://doi.org/10.1103/PhysRevA.85.033620)
8. A. Dauphin, N. Goldman, Extracting the Chern number from the dynamics of a Fermi gas: Implementing a quantum Hall bar for cold atoms. *Phys. Rev. Lett.* **111**, 135302 (2013). [Medline doi:10.1103/PhysRevLett.111.135302](https://doi.org/10.1103/PhysRevLett.111.135302)
9. D. A. Abanin, T. Kitagawa, I. Bloch, E. Demler, Interferometric approach to measuring band topology in 2D optical lattices. *Phys. Rev. Lett.* **110**, 165304 (2013). [Medline doi:10.1103/PhysRevLett.110.165304](https://doi.org/10.1103/PhysRevLett.110.165304)
10. P. Hauke, M. Lewenstein, A. Eckardt, Tomography of band insulators from quench dynamics. *Phys. Rev. Lett.* **113**, 045303 (2014). [Medline doi:10.1103/PhysRevLett.113.045303](https://doi.org/10.1103/PhysRevLett.113.045303)
11. M. Atala, M. Aidelsburger, J. T. Barreiro, D. Abanin, T. Kitagawa, E. Demler, I. Bloch, Direct measurement of the Zak phase in topological Bloch bands. *Nat. Phys.* **9**, 795–800 (2013). [doi:10.1038/nphys2790](https://doi.org/10.1038/nphys2790)
12. A. H. Castro Neto, F. Guinea, N. M. R. Peres, K. S. Novoselov, A. K. Geim, The electronic properties of graphene. *Rev. Mod. Phys.* **81**, 109–162 (2009). [doi:10.1103/RevModPhys.81.109](https://doi.org/10.1103/RevModPhys.81.109)
13. See the supplementary materials on *Science Online*.
14. G. P. Mikitik, Y. V. Sharlai, Manifestation of Berry’s phase in metal physics. *Phys. Rev. Lett.* **82**, 2147–2150 (1999). [doi:10.1103/PhysRevLett.82.2147](https://doi.org/10.1103/PhysRevLett.82.2147)
15. Y. Zhang, Y.-W. Tan, H. L. Stormer, P. Kim, Experimental observation of the quantum Hall effect and Berry’s phase in graphene. *Nature* **438**, 201–204 (2005). [Medline doi:10.1038/nature04235](https://doi.org/10.1038/nature04235)

16. K. S. Novoselov, A. K. Geim, S. V. Morozov, D. Jiang, M. I. Katsnelson, I. V. Grigorieva, S. V. Dubonos, A. A. Firsov, Two-dimensional gas of massless Dirac fermions in graphene. *Nature* **438**, 197–200 (2005). [Medline doi:10.1038/nature04233](#)
17. Y. Liu, G. Bian, T. Miller, T.-C. Chiang, Visualizing electronic chirality and Berry phases in graphene systems using photoemission with circularly polarized light. *Phys. Rev. Lett.* **107**, 166803 (2011). [Medline doi:10.1103/PhysRevLett.107.166803](#)
18. C. Hwang, C.-H. Park, D. A. Siegel, A. V. Fedorov, S. G. Louie, A. Lanzara, Direct measurement of quantum phases in graphene via photoemission spectroscopy. *Phys. Rev. B* **84**, 125422 (2011). [doi:10.1103/PhysRevB.84.125422](#)
19. M. Aidelsburger, M. Lohse, C. Schweizer, M. Atala, J. T. Barreiro, S. Nascimbène, N. R. Cooper, I. Bloch, N. Goldman, Measuring the Chern number of Hofstadter bands with ultracold bosonic atoms. arXiv:1407.4205 (2014); <http://arxiv.org/abs/1407.4205>
20. G. Jotzu, M. Messer, R. Desbuquois, M. Lebrat, T. Uehlinger, D. Greif, T. Esslinger, Experimental realization of the topological Haldane model with ultracold fermions. *Nature* **515**, 237–240 (2014). [Medline doi:10.1038/nature13915](#)
21. I. B. Spielman, Detection of topological matter with quantum gases. *Annalen der Physik* **525**, 797–807 (2013). [doi:10.1002/andp.201300110](#)
22. M. Aidelsburger, M. Atala, S. Nascimbène, S. Trotzky, Y. A. Chen, I. Bloch, Experimental realization of strong effective magnetic fields in an optical lattice. *Phys. Rev. Lett.* **107**, 255301 (2011). [Medline doi:10.1103/PhysRevLett.107.255301](#)
23. L. Tarruell, D. Greif, T. Uehlinger, G. Jotzu, T. Esslinger, Creating, moving and merging Dirac points with a Fermi gas in a tunable honeycomb lattice. *Nature* **483**, 302–305 (2012). [Medline doi:10.1038/nature10871](#)
24. J. Struck, M. Weinberg, C. Ölschläger, P. Windpassinger, J. Simonet, K. Sengstock, R. Höppner, P. Hauke, A. Eckardt, M. Lewenstein, L. Mathey, Engineering Ising-XY spin-models in a triangular lattice using tunable artificial gauge fields. *Nat. Phys.* **9**, 738–743 (2013). [doi:10.1038/nphys2750](#)
25. M. Aidelsburger, M. Atala, M. Lohse, J. T. Barreiro, B. Paredes, I. Bloch, Realization of the Hofstadter Hamiltonian with ultracold atoms in optical lattices. *Phys. Rev. Lett.* **111**, 185301 (2013). [Medline doi:10.1103/PhysRevLett.111.185301](#)
26. H. Miyake, G. A. Siviloglou, C. J. Kennedy, W. C. Burton, W. Ketterle, Realizing the Harper Hamiltonian with laser-assisted tunneling in optical lattices. *Phys. Rev. Lett.* **111**, 185302 (2013). [Medline doi:10.1103/PhysRevLett.111.185302](#)
27. N. Goldman, G. Juzeliunas, P. Ohberg, I. B. Spielman, Light-induced gauge fields for ultracold atoms. arXiv:1308.6533 (2013).
28. M. Ben Dahan, E. Peik, J. Reichel, Y. Castin, C. Salomon, Bloch oscillations of atoms in an optical potential. *Phys. Rev. Lett.* **76**, 4508–4511 (1996). [Medline doi:10.1103/PhysRevLett.76.4508](#)
29. M. Greiner, I. Bloch, O. Mandel, T. W. Hänsch, T. Esslinger, Exploring phase coherence in a 2D lattice of Bose-Einstein condensates. *Phys. Rev. Lett.* **87**, 160405 (2001). [Medline doi:10.1103/PhysRevLett.87.160405](#)

30. S.-L. Zhu, B. Wang, L.-M. Duan, Simulation and detection of Dirac fermions with cold atoms in an optical lattice. *Phys. Rev. Lett.* **98**, 260402 (2007). [Medline](#)  
[doi:10.1103/PhysRevLett.98.260402](https://doi.org/10.1103/PhysRevLett.98.260402)
31. P. Dietl, F. Piéchon, G. Montambaux, New magnetic field dependence of Landau levels in a graphenelike structure. *Phys. Rev. Lett.* **100**, 236405 (2008). [Medline](#)  
[doi:10.1103/PhysRevLett.100.236405](https://doi.org/10.1103/PhysRevLett.100.236405)
32. L. Fallani, L. De Sarlo, J. E. Lye, M. Modugno, R. Saers, C. Fort, M. Inguscio, Observation of dynamical instability for a Bose-Einstein condensate in a moving 1D optical lattice. *Phys. Rev. Lett.* **93**, 140406 (2004). [Medline](#) [doi:10.1103/PhysRevLett.93.140406](https://doi.org/10.1103/PhysRevLett.93.140406)
33. C. D’Errico, M. Zaccanti, M. Fattori, G. Roati, M. Inguscio, G. Modugno, A. Simoni, Feshbach resonances in ultracold  $^{39}\text{K}$ . *New J. Phys.* **9**, 223 (2007). [doi:10.1088/1367-2630/9/7/223](https://doi.org/10.1088/1367-2630/9/7/223)
34. I. Carusotto, C. Ciuti, Quantum fluids of light. *Rev. Mod. Phys.* **85**, 299–366 (2013).  
[doi:10.1103/RevModPhys.85.299](https://doi.org/10.1103/RevModPhys.85.299)
35. F. Grusdt, D. Abanin, E. Demler, Measuring  $Z_2$  topological invariants in optical lattices using interferometry. *Phys. Rev. A* **89**, 043621 (2014). [doi:10.1103/PhysRevA.89.043621](https://doi.org/10.1103/PhysRevA.89.043621)
36. P. Zanardi, M. Rasetti, Holonomic quantum computation. *Phys. Lett. A* **264**, 94–99 (1999).  
[doi:10.1016/S0375-9601\(99\)00803-8](https://doi.org/10.1016/S0375-9601(99)00803-8)
37. S. A. Parameswaran, R. Roy, S. L. Sondhi, Fractional quantum Hall physics in topological flat bands. *C. R. Phys.* **14**, 816–839 (2013). [doi:10.1016/j.crhy.2013.04.003](https://doi.org/10.1016/j.crhy.2013.04.003)
38. A. K. Tuchman, M. A. Kasevich, Phase-slip interferometry for precision force measurements. *Phys. Rev. Lett.* **103**, 130403 (2009). [Medline](#)  
[doi:10.1103/PhysRevLett.103.130403](https://doi.org/10.1103/PhysRevLett.103.130403)
39. D. Xiao, M.-C. Chang, Q. Niu, Berry phase effects on electronic properties. *Rev. Mod. Phys.* **82**, 1959–2007 (2010). [doi:10.1103/RevModPhys.82.1959](https://doi.org/10.1103/RevModPhys.82.1959)
40. G. W. Semenoff, Condensed-matter simulation of a three-dimensional anomaly. *Phys. Rev. Lett.* **53**, 2449–2452 (1984). [doi:10.1103/PhysRevLett.53.2449](https://doi.org/10.1103/PhysRevLett.53.2449)
41. Y. Aharonov, L. Susskind, Observability of the sign change of spinors under  $2\pi$  rotations. *Phys. Rev.* **158**, 1237–1238 (1967). [doi:10.1103/PhysRev.158.1237](https://doi.org/10.1103/PhysRev.158.1237)
42. G. P. Mikitik, Y. V. Sharlai, Manifestation of Berry’s phase in metal physics. *Phys. Rev. Lett.* **82**, 2147–2150 (1999). [doi:10.1103/PhysRevLett.82.2147](https://doi.org/10.1103/PhysRevLett.82.2147)
43. L. Tarruell, D. Greif, T. Uehlinger, G. Jotzu, T. Esslinger, Creating, moving and merging Dirac points with a Fermi gas in a tunable honeycomb lattice. *Nature* **483**, 302–305 (2012). [Medline](#) [doi:10.1038/nature10871](https://doi.org/10.1038/nature10871)
44. G. Montambaux, F. Piéchon, J.-N. Fuchs, M. O. Goerbig, Merging of Dirac points in a two-dimensional crystal. *Phys. Rev. B* **80**, 153412 (2009). [doi:10.1103/PhysRevB.80.153412](https://doi.org/10.1103/PhysRevB.80.153412)
45. S. K. Baur, M. H. Schleier-Smith, N. R. Cooper, Dynamic optical superlattices with topological bands. *Phys. Rev. A* **89**, 051605 (2014). [doi:10.1103/PhysRevA.89.051605](https://doi.org/10.1103/PhysRevA.89.051605)

46. T. Fukui, Y. Hatsugai, H. Suzuki, Chern numbers in discretized Brillouin zone: Efficient Method of computing (spin) Hall conductances. *J. Phys. Soc. Jpn.* **74**, 1674–1677 (2005). [doi:10.1143/JPSJ.74.1674](https://doi.org/10.1143/JPSJ.74.1674)
47. L. Fallani, L. De Sarlo, J. E. Lye, M. Modugno, R. Saers, C. Fort, M. Inguscio, Observation of dynamical instability for a Bose-Einstein condensate in a moving 1D optical lattice. *Phys. Rev. Lett.* **93**, 140406 (2004). [Medline doi:10.1103/PhysRevLett.93.140406](https://doi.org/10.1103/PhysRevLett.93.140406)
48. A. Zenesini, D. Ciampini, O. Morsch, E. Arimondo, Observation of Stückelberg oscillations in accelerated optical lattices. *Phys. Rev. A* **82**, 065601 (2010). [doi:10.1103/PhysRevA.82.065601](https://doi.org/10.1103/PhysRevA.82.065601)
49. M. Ben Dahan, E. Peik, J. Reichel, Y. Castin, C. Salomon, Bloch oscillations of atoms in an optical potential. *Phys. Rev. Lett.* **76**, 4508–4511 (1996). [Medline doi:10.1103/PhysRevLett.76.4508](https://doi.org/10.1103/PhysRevLett.76.4508)